CHEMISTRY

Surrounded catalysts prepared by ion-exchange inverse loading

Panpan Hao[1], Mingjiang Xie[1], Shanyong Chen[1], Muhong Li[1], Feifei Bi[1], Yu Zhang[1], Ming Lin[2], Xiangke Guo[1], Weiping Ding[1], Xuefeng Guo[1]*

The supported catalyst featuring highly dispersed active phase on support is the most important kind of industrial catalyst. Extensive research has demonstrated the critical role (in catalysis) of the interfacial interaction/perimeter sites between the active phase and support. However, the supported catalyst prepared by traditional methods generally presents low interface density because of limit contact area. Here, an ion-exchange inverse loading (IEIL) method has been developed, in which the precursor of support is controllably deposited onto the precursor of active phase by ion-exchange reaction, leading to an active core surrounded (by support) catalyst with various structures. The unique surrounded structure presents not only high interface density and mutually changed interface but also high stability due to the physical isolation of active phase, revealing superior catalytic performances to the traditional supported catalysts, suggesting the great potential of this new surrounded catalyst as the upgrade of supported catalyst in heterogeneous catalysis.

INTRODUCTION

Heterogeneous catalysis has been considered as the heart of the modern energy and chemical industries (1). In the practical application, supported catalysts are the most widely used type of heterogeneous catalysts, in which the active phase/particles are located on a mostly high–surface area support to enhance the thermal stability and mechanical strength of the catalysts and simultaneously reduce the dosage of active species (2). In many cases, the supports are not only a matrix to disperse the active phases/particles; they could even exert a more important influence on a reaction process by adjusting the electronic and geometrical structure of the active phase (3). In the late 1970s, a concept of "strong metal-support interaction (SMSI)" based on the metal supported on transition metal oxides (TMOs), proposed by Tauster *et al.* (4), provoked great attention to the prominent role that the interface interaction can play in the reaction. Strong interface interaction between the active phase and support can even change the geometric/electronic structures of not only the active phase but also the support at the interface, creating unique interfacial perimeter sites. Recently, extensive research has demonstrated the critical role in catalysis of the interfacial perimeter sites (5–25). Cargnello *et al.* (5) found that CO oxidation on ceria-based catalysts was greatly enhanced at the ceria-metal interface sites for a range of group VIII metal (Ni, Pt, and Pd) catalysts, with a direct participation in the reaction of metal atoms at the perimeter and ceria surface oxygen. Kattel *et al.* (6) identified the active sites over commercial $Cu/ZnO/Al_2O_3$ catalysts for CO_2 hydrogenation to methanol, highlighting a synergy of Cu and ZnO at the interface (ZnO-Cu interfacial sites) that facilitated methanol synthesis, rather than the Zn-Cu bimetallic sites. Fu *et al.* (11) proposed that highly dispersed TMO nanostructure deliberately constructed on the surface of noble metals (NMs) maximized the density of metal-oxide interfaces, and the fabricated TMO-NM interfaces exerted a unique chemical environment to confine the active metal centers so

that the coordinatively unsaturated active sites can be stabilized and demonstrated extraordinary performance in low-temperature catalytic oxidation reactions. Xu *et al.* (22) demonstrated that encapsulating copper phyllosilicate nanotubes with mesoporous SiO_2 created a practical Cu nanocatalyst with abundant $Cu-O-SiO_x$ interfacial perimeter sites, which exhibited the best performance in catalytic hydrogenation of esters among all reported Cu catalysts. Most recently, Cao *et al.* (25) created atomically dispersed iron hydroxide anchored on Pt nanoparticles by using atomic layer deposition to maximize the $Fe_1(OH)_3$-Pt(100) interfacial sites, which played a dominant role in reacting with CO readily and facilitating oxygen activation during the preferential oxidation of CO in H_2 (PROX) reaction, enabling the complete and 100% selective CO removal over a broad operational temperature window. These results highlight the importance of both the interface interaction and the interface area/density for catalytic performances, which are attracting increasing attention in the catalysis field today.

In general, the traditional supported catalysts are prepared via two main preparation methods, i.e., impregnation and precipitation (26). In both of these methods, a metal precursor, mostly an inorganic salt, is used as the starting precursor to deposit the active species onto the outer surface of support (as shown in Fig. 1A). These loading methods normally render limited contact area/density and relatively weak interfacial interaction between the active species and the support, which result in easy aggregation of active species and simultaneously sharp reduction of the interfacial area/density during the pretreatment or the reaction process, further affecting the catalytic performance. Inspired by the structure of natural metalloenzymes, in which the active metal center is surrounded by protein molecules that simultaneously demonstrate very high activity and stability, the highly dispersed active species/nanoparticles are expected to be surrounded by the support, leading to rich interface area/density and enhanced interfacial interaction and the highly improved stability of active species. This surrounded structure may open a way to develop high-performance catalytic materials.

Here, we propose a general and facile strategy, i.e., an ion-exchange inverse loading (IEIL) method, to prepare the surrounded catalysts with large active species–support interface. For a typical metal/metal

[1]Key Lab of Mesoscopic Chemistry, School of Chemistry and Chemical Engineering, Nanjing University, Nanjing 210023, China. [2]Institute of Materials Research and Engineering (IMRE), 2 Fusionopolis Way, Innovis #08-03, Singapore 138634, Singapore.
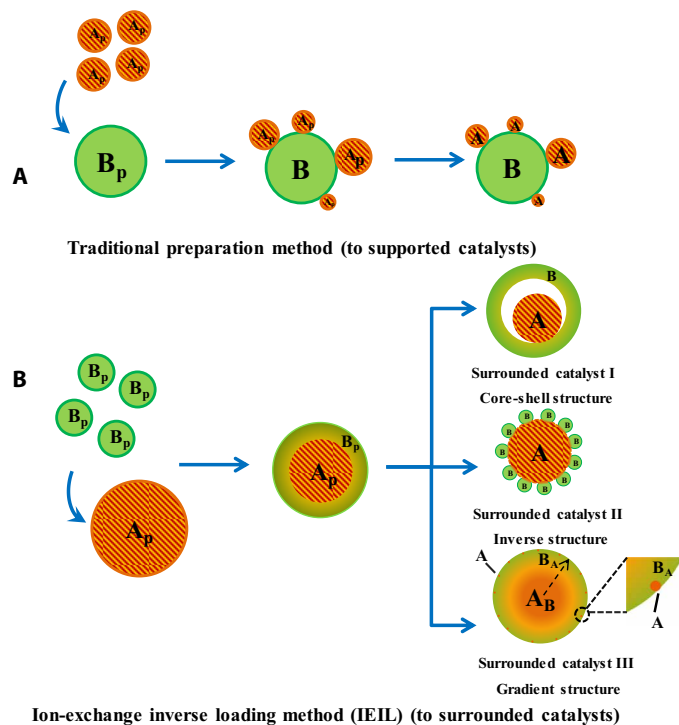*Corresponding author. Email: guoxf@nju.edu.cn

Fig. 1. Schematic of different preparation methods. Schematic diagram of the traditional preparation method (**A**) and ion-exchange inverse loading (IEIL) method (**B**).

oxide catalyst as illustrated in Fig. 1B, a metal hydroxide precursor (A_p, metal ions A^{m+}) is added into the solution of support precursor (B_p, metal ions B^{n+}), and the ion-exchange (IE) reaction takes place driven by the difference of solubility product (K_{sp}). By replacement of metal ion A^{m+} with B^{n+} on the surface of A_p to form $A_p@B_p$ mixed metal hydroxide (MMH) (Fig. 1B), core-shell structured A@B catalyst with high metal-metal oxide interface density and highly dispersed metal nanoparticles can be achieved followed by the subsequent calcination and reduction of $A_p@B_p$ MMH. The degree of ion exchange determines the thickness of B_p, and more importantly, the abundant sources of A_p or B_p contribute to the diversity of the catalyst, suggesting the universality of the IEIL strategy. On the basis of the control over the degree of ion exchange and the various composition of A_p and B_p, the configuration of catalysts can be varied from A@B with core-shell structure to A@B with inverse structure, gradient structure, and so on, all belonging to surrounded (A surrounded by B) catalysts featuring high interface area/density and stability.

Taking the nickel-based surrounded catalyst as a typical example, when A_p represents $Ni(OH)_2$ nanosheet, the replacement of Ni^{2+} with Al^{3+} with a large exchange degree endows the $Ni@Al_2O_3$-IE surrounded catalyst with core-shell structure (surrounded catalyst I, as shown in Fig. 1B), while a small degree of exchange with Ce^{3+} results in the $Ni@CeO_2$-IE surrounded catalyst with inverse structure (surrounded catalyst II, as shown in Fig. 1B). In the case of Cu-rich shell, Ni^{2+} is replaced with Cu^{2+} to achieve the $Ni@Cu$-IE surrounded catalyst with gradient structure (surrounded catalyst III, as shown in Fig. 1B). Compared with the counterpart supported catalysts synthesized by the traditional impregnation method, the obtained surrounded catalysts demonstrate much superior performances in catalytic reactions, such as CO methanation, transfer hydrogenation reaction, etc.

RESULTS

$Ni@Al_2O_3$-IE surrounded catalysts with core-shell structure (for CO methanation) prepared by IEIL method

The catalytic hydrogenation of carbon oxide (CO or CO_2) to produce synthetic natural gas (SNG), known as methanation, is an indispensable process of coal-to-SNG technology in industry. The methanation catalyst should have both high activity and good stability at high temperatures (since the methanation process is an exothermic reaction). Conventional Ni/Al_2O_3 catalysts prepared through the traditional impregnation method usually suffer from rapid deactivation as a result of serious carbon deposition and the sintering of Ni particles during the methanation process (27). Thus, developing an efficient methanation catalyst with simultaneously smaller particle size to resist the coking and high thermal stability to avoid the sintering of Ni particles is highly challenging (28). Figure 2A shows the schematic diagram toward the synthesis of core-shell structured $Ni@Al_2O_3$-IE catalyst by the proposed IEIL strategy. For comparison, conventional Ni/Al_2O_3-IM supported catalyst is also prepared by impregnation (IM) method.

Figure 2 (B to E) shows the morphology evolution from the as-prepared nanosheet $Ni(OH)_2$ precursor to the final core-shell $Ni@Al_2O_3$-IE catalyst. The nickel hydroxide nanosheets process a thickness of ~15 nm (Fig. 2B). After IE reaction with Al^{3+} and the following calcination, the resulted $Ni(OH)_2@Al(OH)_3$ MMH (NiAl-MMH) (Fig. 2C) and $NiO@Al_2O_3$-IE (Fig. 2D) inherit the nanosheet morphology, respectively. After further reduction of $NiO@Al_2O_3$-IE by H_2, the obtained $Ni@Al_2O_3$-IE (Fig. 2E) with nickel loading content of 16 weight % (wt %) (as a typical representative) processes a peapod-like core-shell structure with the nickel nanoparticles (ca. 2.9 ± 0.5 nm) surrounded by an alumina substrate [as shown in the enlarged transmission electron microscopy (TEM) image in Fig. 2F]. The IEIL method shows great advantages for the synthesis of high-loading (even up to 44 wt % Ni) Ni-Al_2O_3 catalyst with highly dispersed Ni nanoparticles (see fig. S1A and section S1). In sharp contrast, the Ni/Al_2O_3-IM sample with the same Ni loading (16 wt %) (see fig. S2A and section S2) prepared by the traditional impregnation method exhibits a random packing of Ni nanoparticles with a very broad particle size distribution (7 to 13 nm) supported on the surface of Al_2O_3. On the basis of the H_2 pulse adsorption, the Ni dispersion of $Ni@Al_2O_3$-IE is 15.0%, three times higher than that of Ni/Al_2O_3-IM (4.6%), which is in good agreement with the much smaller Ni particle size in $Ni@Al_2O_3$-IE.

Figure 2G shows the x-ray diffraction (XRD) patterns of the samples from a nickel hydroxide precursor to $Ni@Al_2O_3$-IE. To demonstrate the structure evolution, a schematic diagram of the formation process of $Ni@Al_2O_3$-IE is proposed in Fig. 3 (A to D). After ion-exchange reaction for a certain period, the obtained MMH precursors (NiAl-MMH) are Ni-Al hydrotalcite-like compounds (as shown in Fig. 2G), in which Ni^{2+} is located mainly in the center while the surface of NiAl-MMH is enriched by Al^{3+}, forming a $Ni(OH)_2@Al(OH)_3$-like gradient structure due to the incomplete IE process (Fig. 3A). After calcination, three new peaks emerged in the calcined $NiO@Al_2O_3$-IE (as shown in Fig. 2G) can be assigned to NiO, which shifted to higher 2θ values than those of pure NiO due to the diffusion of Al^{3+} in NiO (29), forming a mixed oxide (NiAl-MO) phase (Fig. 3B). During the reduction process by H_2, Ni^{2+} is reduced to form metallic Ni centers accompanied by the migration of Ni^{2+} from NiAl-MO phase, resulting in the crystallization of residual alumina (Fig. 3, C and D). However, the reduction of Ni^{2+} in the
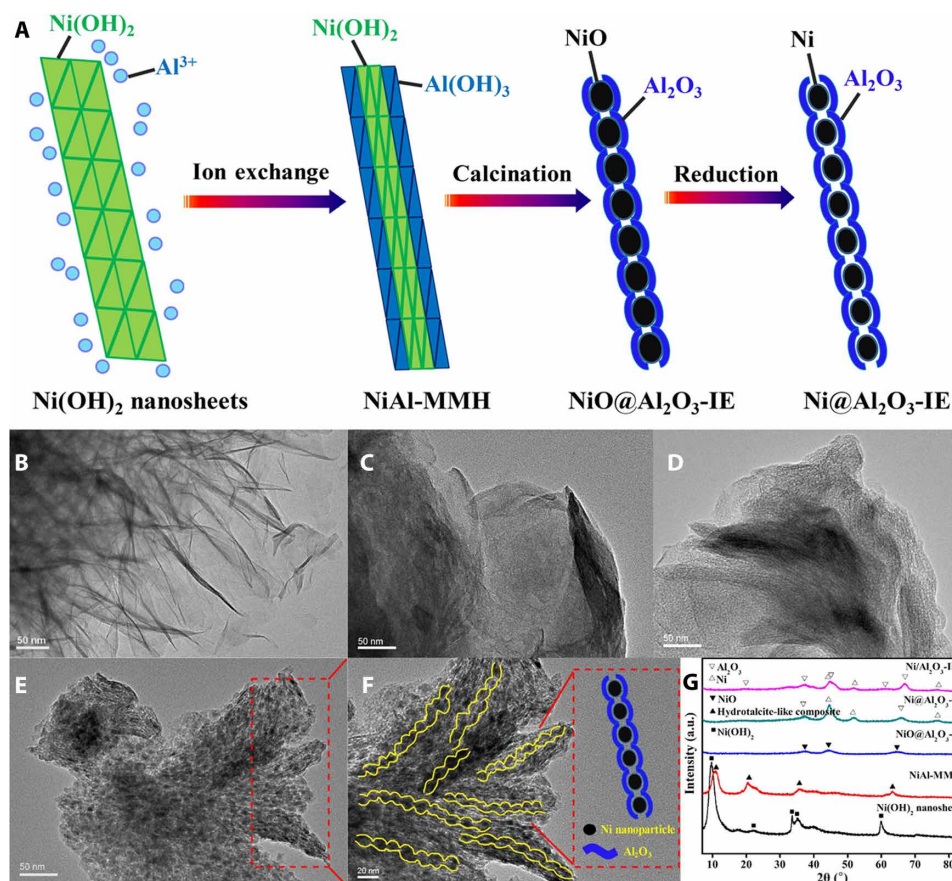
Fig. 2. Schematic and microscopic characterizations of catalysts. (**A**) Schematic diagram toward the synthesis of peapod-like Ni@Al$_2$O$_3$-IE surrounded catalyst via the IEIL method. Transmission electron microscopy images of (**B**) Ni(OH)$_2$ precursor, (**C**) NiAl-MMH, (**D**) NiO@Al$_2$O$_3$-IE, (**E** and **F**) Ni@Al$_2$O$_3$-IE, and (**G**) x-ray diffraction patterns of the different products. a.u., arbitrary units.

NiAl-MO phase is generally hindered by alumina, and as a consequence, the residual Ni^{2+} in Al$_2$O$_3$ shifts the reflections of Al$_2$O$_3$ to lower 2θ values compared to those of the commercial pure γ-Al$_2$O$_3$ and Ni/Al$_2$O$_3$-IM as shown in Fig. 2G. In contrast, the migration of Ni^{2+} to γ-Al$_2$O$_3$ (Fig. 3E) in Ni/Al$_2$O$_3$-IM prepared by impregnation is ignorable (Fig. 3, F and G) because of the weak interface interaction between Ni precursor and the inert γ-Al$_2$O$_3$ support. The obvious differences both in structure and composition (as shown in Fig. 3, D and G) highlight the unique features and advantages of the surrounded catalyst prepared by IEIL method with active core surrounded structure and mutually (active core and support) changed interfaces (generally resulting in stronger interaction) compared to the normal supported catalyst prepared by the traditional methods.

The nitrogen sorption isotherm of Ni@Al$_2$O$_3$-IE displays a type IV isotherm with a H$_2$-type hysteresis loop at a relative pressure (P/P_0) of 0.4 to 0.6 (Fig. 3H), revealing the presence of mesoporous structure. The specific Brunauer-Emmett-Teller surface area of Ni@Al$_2$O$_3$-IE is 184 m^2 g^{-1}, and the average pore size calculated by the Barrett-Joyner-Halenda method is around 3.7 nm (Fig. 3H, inset). In a typical synthesis, after IE process and calcination, core-shell structured NiO@Al$_2$O$_3$-IE mixed metal oxide precursor can be obtained. During the subsequent reduction by H$_2$, the Al$_2$O$_3$ shell basically remains unchanged, while NiO is reduced to metallic Ni accompanied with the volume shrinkage, leading to abundant porosity that

is responsible for the mesopores existed in Ni@Al$_2$O$_3$-IE (Fig. 3H). Therefore, the average pore diameter of 3.7 nm corresponds to the average particle size of the original NiO encapsulated by Al$_2$O$_3$ shell. On the basis of the XRD results, when cubic NiO is reduced to cubic Ni, the cell volume shrinks by 40% theoretically. According to the theoretical calculation, NiO with diameter of 3.7 nm will shrink to 3.1 nm after reduction to Ni by assuming spherical shape of NiO and Ni particles. The calculated result (3.1 nm) accords well with the mean particle size of metal nickel (2.9 nm) measured by TEM, confirming the formation of york-shell–like structure of Ni@Al$_2$O$_3$-IE. In sharp contrast, the nitrogen sorption isotherm of Ni/Al$_2$O$_3$-IM exhibits a H3-type hysteresis at a relative pressure (P/P_0) of 0.7 to 1.0 (see fig. S2B and section S2), indicating the presence of slit-like pore that is caused by the stacking of Al$_2$O$_3$ support. In addition, the pore size distribution is broad (mean pore size of 29.4 nm) because of the disordered stacking of Al$_2$O$_3$ support particles (fig. S2B).

On the basis of the CO temperature-programmed desorption (CO-TPD) results (fig. S2C), Ni@Al$_2$O$_3$-IE presents strong CO desorption peaks, indicating the feasible CO adsorption on Ni surface. In addition, CO desorption temperature of the Ni@Al$_2$O$_3$-IE surrounded catalyst shifts toward lower temperature compared with the traditional Ni/Al$_2$O$_3$-IM supported catalyst, demonstrating that CO molecules are easier to be desorbed on Ni@Al$_2$O$_3$-IE, which may be attributed to the confinement effect of the core-shell structure of Ni@Al$_2$O$_3$-IE (*30, 31*).
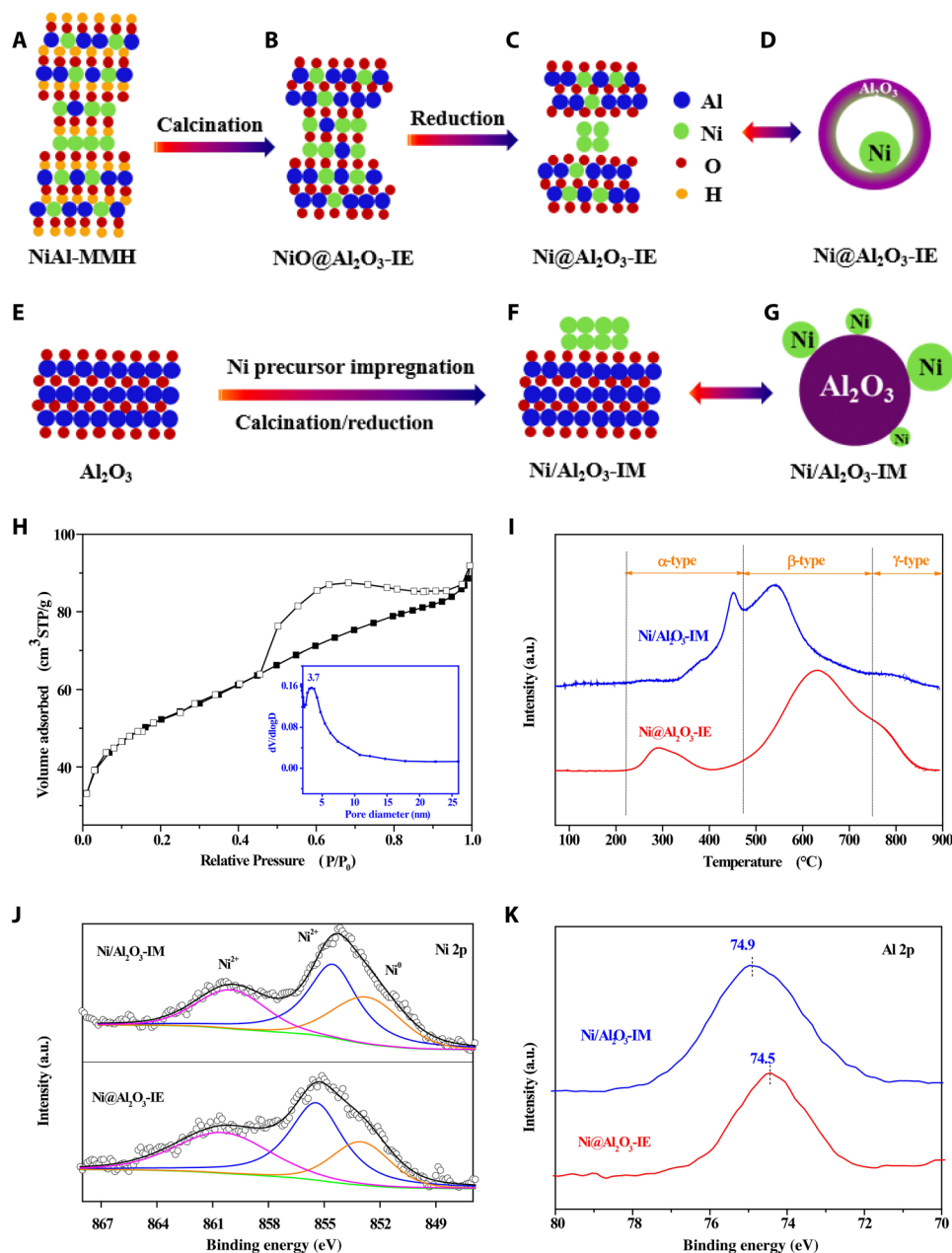
Fig. 3. Detailed structure characterizations of catalysts. Schematic diagrams of the proposed formation process of Ni@Al$_2$O$_3$-IE (**A** to **D**) and Ni/Al$_2$O$_3$-IM (**E** to **G**). (**H**) Nitrogen sorption isotherms and the pore-size distribution (inset) of Ni@Al$_2$O$_3$-IE (Standard temperature pressure, STP). H$_2$ temperature-programmed reduction profiles (**I**) and Ni 2p (**J**) and Al 2p (**K**) x-ray photoelectron spectra of Ni@Al$_2$O$_3$-IE and Ni/Al$_2$O$_3$-IM.

The reducibility of nickel species in Ni@Al$_2$O$_3$-IE are further investigated by H$_2$ temperature-programmed reduction (H$_2$-TPR) (Fig. 3I). Three hydrogen consumption peaks denoted as α-, β-, and γ-type can be assigned to the reduction of NiO with small particle size, less reducible NiO in MO phase, and stable nickel aluminate phase with the spinel structure, respectively (*32*). Compared to Ni/Al$_2$O$_3$-IM, α-type NiO in Ni@Al$_2$O$_3$-IE is obviously more active and the reduction temperature decreases from 450 to ~300°C, implying the presence of highly dispersed NiO species with smaller particle size, which is responsible for the excellent low-temperature catalytic activity. The β-type NiO is

dominant in Ni@Al$_2$O$_3$-IE, and the peak shifts toward higher temperature, suggesting that the interaction between NiO and Al$_2$O$_3$ is stronger in the NiAl-MO phase than that in Ni/Al$_2$O$_3$-IM, confirming the mutually (NiO and Al$_2$O$_3$) changed interfaces in NiO@Al$_2$O$_3$-IE. The Ni^{2+} contribution in x-ray photoelectron spectra (XPS) (Fig. 3J) shifts to higher binding energy in Ni@Al$_2$O$_3$-IE (855.3 eV) than that in Ni/Al$_2$O$_3$-IM (854.7 eV); simultaneously, the peak assigned to Al^{3+} in Al$_2$O$_3$ (Fig. 3K) shifts toward lower binding energy in Ni@Al$_2$O$_3$-IE (74.5 eV) than that in Ni/Al$_2$O$_3$-IM (74.9 eV), further confirming the strong interaction between Ni species and alumina in Ni@Al$_2$O$_3$-IE.
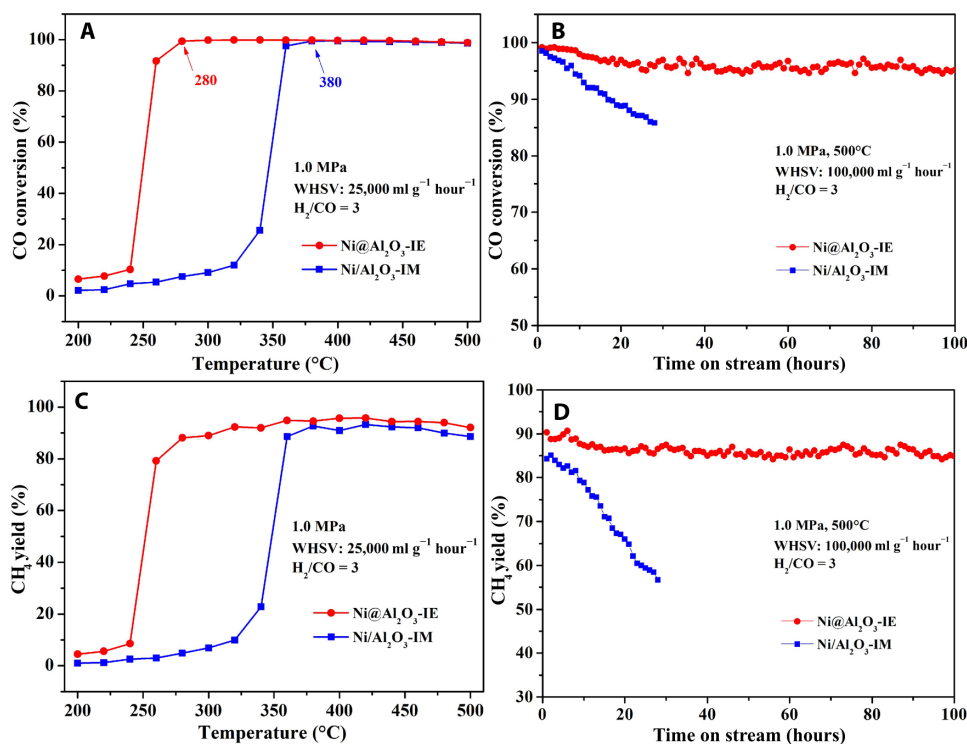
Fig. 4. Catalytic performance of catalysts. (**A** and **B**) CO conversion and (**C** and **D**) CH$_4$ yield of Ni/Al$_2$O$_3$-IM and Ni@Al$_2$O$_3$-IE.

The catalytic performances of Ni@Al$_2$O$_3$-IE and Ni/Al$_2$O$_3$-IM toward CO methanation reaction are shown in Fig. 4 (A to D) and fig. S3. The value of T_{100}, corresponding to the temperature at which 100% conversion is obtained, is 380°C for Ni/Al$_2$O$_3$-IM, while the CO conversion on Ni@Al$_2$O$_3$-IE exceeds 90% at 260°C and reaches 100% at 280°C (Fig. 4A). On the basis of the results of H$_2$ chemisorption and the CO conversion at 280°C under a high weight hourly space velocity (WHSV) of 100,000 ml g^{-1} hour^{-1}, the turnover frequency (TOF)$_{CO,280}$ values of Ni@Al$_2$O$_3$-IE is 3.7 s^{-1}, six times higher than that of Ni/Al$_2$O$_3$-IM (0.6 s^{-1}), further confirming the superior catalytic activity of the Ni@Al$_2$O$_3$-IE catalyst. In the lifetime test, the Ni@Al$_2$O$_3$-IE catalyst exhibits simultaneously high stability and high yield (without obvious decline) during 100 hours at 500°C with a high space velocity of 100,000 ml g^{-1} hour^{-1} (Fig. 4, B and D). In sharp contrast, the activity of the Ni/Al$_2$O$_3$-IM has a remarkable decline after only 30 hours, and the reaction had to be stopped because of the serious plugging of the reactor by coke. The carbon content of the used catalysts after CO methanation is 4.9 and 17.5 wt % for Ni@Al$_2$O$_3$-IE-100h and Ni/Al$_2$O$_3$-IM-30h, respectively, indicating much better anti-coking property of Ni@Al$_2$O$_3$-IE (see fig. S4A and section S4). The NH$_3$-TPD results (see fig. S2D and section S2) of Ni@Al$_2$O$_3$-IE indicate that the strong interaction of Ni and Al$_2$O$_3$ lowers the acid amount, which may contribute to the anti-coking performance. The morphology and crystallinity of the used catalyst are characterized and analyzed (see fig. S4 and section S4), and the results further confirms that the coke formation and Ni particle growth have been strongly suppressed on Ni@Al$_2$O$_3$-IE surrounded catalyst. In general, for Ni-based catalysts for methanation, the smaller Ni nanoparticles, the higher activity and less coke, but along with worse stability due to the sintering of high-active nanoparticles (*33*). In the present Ni@Al$_2$O$_3$-IE surrounded catalyst, the physical

isolation of Ni nanoparticles by Al$_2$O$_3$ shell not only offers a large surface area for the high dispersion of active metal but also exerts a spatial restriction on these nickel nanoparticles, hampering their sintering and coke formation in the long-term employment even under harsher conditions (*12*), displaying the advanced structural design and much superior catalytic performances.

Ni@CeO$_2$-IE surrounded catalysts with inverse structure (for catalytic transfer hydrogenation) prepared by IEIL method
Catalytic transfer hydrogenation opens up a new dimension in reduction of organic compounds because of operational safety and enhanced degree of control in selectivity compared with the conventional molecular hydrogen–based process. Non-NM catalysts as an alternative for precious metals have attracted extensive attention due to their low cost and abundance but suffering from their relatively poor catalytic activity and selectivity (*34*). In this context, we fabricate an inverse structure with Ni particles surrounded by CeO$_2$ nanoparticles (denoted as Ni@CeO$_2$-IE; see Fig. 5, B and C, and fig. S5 in section S5) via IEIL strategy, and the schematic diagram of the synthesis is displayed in Fig. 5A. The CeO$_2$ support is expected to improve the catalytic activity/selectivity via participating in the reaction process (*19*). For comparison, Ni/CeO$_2$-IM supported catalyst is prepared by the traditional impregnation method.

For the transfer hydrogenation of nitrobenzene with hydrazine to aniline, the Ni@CeO$_2$-IE surrounded catalyst (Ce/Ni molar ratio of 0.02, Fig. 5, B and C) shows complete conversion of nitrobenzene and 100% selectivity to aniline at 60°C for 1 hour, while Ni/CeO$_2$-IM displays a poor activity (nitrobenzene conversion of 38%) with an aniline selectivity of 76%, eventually only giving an aniline yield of 29% under the same reaction conditions (Fig. 5D). The other products detected by gas chromatography (GC) are nitrosobenzene
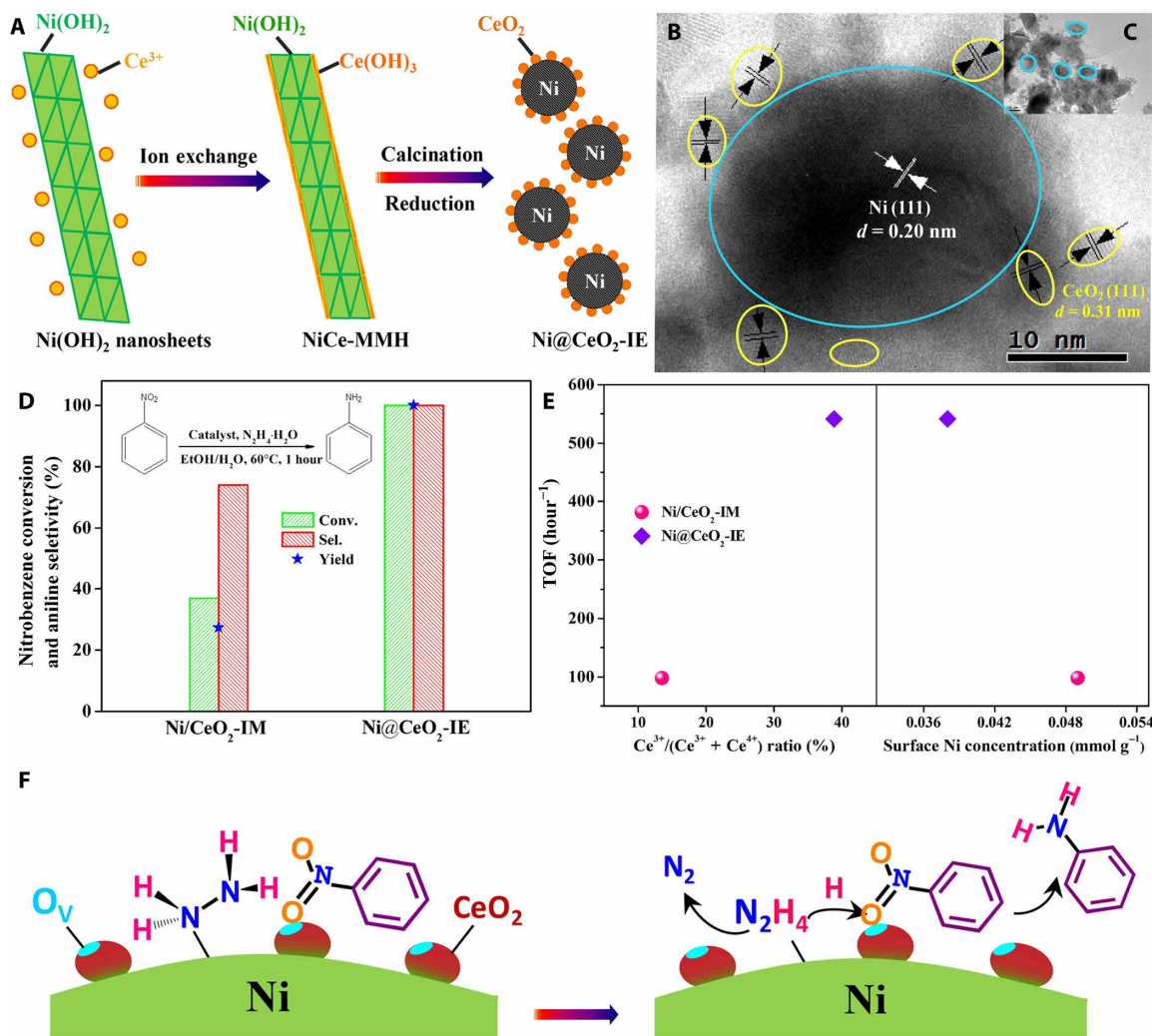
Fig. 5. Schematic, characterizations and performances of catalysts. (**A**) Schematic diagram toward the synthesis of Ni@CeO$_2$-IE surrounded catalyst via the IEIL method. (**B** and **C**) TEM images of Ni@CeO$_2$-IE (Ce/Ni molar ratio of 0.02). (**D**) Catalytic performances of Ni/CeO$_2$-IM and Ni@CeO$_2$-IE catalysts. (**E**) TOF as a function of surface Ni concentration and Ce^{3+}/(Ce^{3+} + Ce^{4+}) ratio. (**F**) The possible synergic catalysis mechanism on Ni@CeO$_2$-IE surrounded catalyst.

(NSB) with a selectivity of 6% and azoxybenzene (AOB) with a selectivity of 18%. In addition, the TOF value of Ni@CeO$_2$-IE (541.6 hour^{-1}) is 5.5 times larger than that of Ni/CeO$_2$-IM (97.9 hour^{-1}), although the later has higher surface Ni concentration (0.038 mmol g^{-1} versus 0.049 mmol g^{-1}) (Fig. 5E), indicating that Ni particles do not serve as the sole active site. The further investigation discovers a positive relationship between the TOF value and Ce^{3+}/(Ce^{3+} + Ce^{4+}) ratio (see Fig. 5E, fig. S6A, and section S6). The larger Ce^{3+}/(Ce^{3+} + Ce^{4+}) ratio suggests more oxygen vacancies (O$_v$) in CeO$_2$ (XPS results, fig. S6, B to E). Benefiting from the special IEIL method, the obtained mixed metal oxide after calcination usually processes mutually changed interface, which enhances the interaction between Ni^{2+} and CeO$_2$, resulting in the incorporation of more Ni^{2+} ions into the CeO$_2$ lattice. The lattice distortion and the enhancement of oxygen mobility benefit the formation of more oxygen vacancies. In contrast, the interfacial interaction on the traditional supported catalyst prepared by impregnation is generally weak. Therefore, the reduced Ni@CeO$_2$-IE surrounded catalyst processes larger Ce^{3+}/

(Ce^{3+} + Ce^{4+}) ratio and more oxygen vacancies than those of Ni/CeO$_2$-IM supported catalyst (Fig. 5E and fig. S6).

On the basis of the catalytic performances and XPS results, the Ni-CeO$_2$ interfacial perimeter sites may serve as synergistic sites in nitrobenzene reduction reaction. Since Ni@CeO$_2$-IE has higher vacancy concentration (2.34 times more than those of Ni/CeO$_2$-IM), the oxygen vacancies serve as the adsorption sites for the highly preferential adsorption of nitrobenzene (35, 36), while Ni serves as the active site for N$_2$H$_4$ dissociation and produces the active hydrogen species, which easily spill over to the neighboring interface of CeO$_2$ to reduce the adsorbed nitrobenzene. After the complete hydrogenation by the active spilled-over hydrogen, the resulted aniline can be desorbed from CeO$_2$ support, realizing the superior catalytic activity and selectivity of Ni@CeO$_2$-IE surrounded catalysts. In contrast, when Ni/CeO$_2$-IM with low oxygen vacancy concentration and high surface Ni concentration is used as a catalyst, nitro group of nitrobenzene will be adsorbed on both the surface of Ni nanoparticles and the surface of CeO$_2$ support. N$_2$H$_4$ activation on Ni

nanoparticles produces active hydrogen species, allowing the stepwise reduction of nitrobenzene adsorbed on Ni particles to NSB, hydroxylamine intermediate, and the final product aniline. However, in this case, the coadsorption of these two intermediates and subsequent coupling reactions between them into the by-product of AOB will occur readily, leading to the poor aniline selectivity. Furthermore, the Ni@CeO$_2$-IE surrounded catalyst could be recycled at least six times with initial catalytic activity (see fig. S7 and section S7), revealing its high stability; in sharp contrast, the activity of supported Ni/CeO$_2$-IM catalyst declined from 38 to 15% after six runs, which highlights the strong interaction (stability) between Ni and CeO$_2$ in the Ni@CeO$_2$-IE surrounded structure derived from ion exchange.

Ni@Cu-IE surrounded catalysts with gradient structure (for semihydrogenation of phenylacetylene) prepared by IEIL method

Besides core-shell and inverse structure, when Cu^{2+} is used to exchange with Ni(OH)$_2$ through IEIL method, a gradient alloy structure varied from nickel-rich core to copper-rich surface can be formed (Fig. 6). The as-prepared Ni@Cu-IE catalyst (see fig. S8 and section S8) exhibits outstanding styrene selectivity (90%) during the semihydrogenation of phenylacetylene (see table S1 for more catalytic data), even better than some supported NM catalyst such as nano-Pd/Al$_2$O$_3$ catalyst (60%) at the complete conversion of phenylacetylene (37).

The formation of different surrounded structure mainly depends on the exchange degree of the metal hydroxide precursor (A$_p$, metal ions A^{m+}) with support precursor (B$_p$, metal ions B^{n+}) and the inherent properties of both metal precursor and oxide support precursor (e.g., reducibility). In general, when the ion exchange degree is little, A@B surrounded catalyst with inverse structure can be obtained, while when metal ion A^{m+} is exchanged with B^{n+} in a large degree, core-shell structured A@B surrounded catalyst will be achieved (see fig. S9 and section S9). However, once the oxide surrounding layer and the metal core precursor are thermodynamically susceptible to be reduced to the metallic state simultaneously, gradient alloy structure will be obtained ultimately, as in the case of Ni@Cu-IE. The above examples well demonstrate the universality of IEIL strategy, which paves the new way to controllably fabricate a variety of catalytic materials with various surrounded structures in which high activity and stability can be achieved simultaneously, far superior to

their traditional supported counterparts, highlighting the importance of this IEIL strategy for the design of advanced catalysts.

DISCUSSION

In summary, on the basis of the importance of metal/oxide interface in catalysis, an IEIL strategy has been developed to controllably synthesize various surrounded catalysts (active phase surrounded by support) with large interface area/density and enhanced interface interaction. By controlling the degree of ion exchange and the different precursor species, a series of surrounded catalysts with various structures—such as core-shell, inverse structure, and gradient structure—can be successfully designed and fabricated. Compared to the counterpart traditional supported catalyst, the as-prepared surrounded catalyst shows superior catalytic performance and excellent stability due to the highly enhanced interface area/density and interaction and the physical isolation. This work presents fresh concepts and strategies for the design and fabrication of advanced core-surrounded heterostructures and thus opens up a new way for the targeted development of high-performance catalysts.

MATERIALS AND METHODS
Preparation of Ni(OH)$_2$ nanosheets

The Ni(OH)$_2$ nanosheets were prepared according to our previous work with some modifications (38). In a typical synthesis, commercial MgO (1.6 g) was immersed in a solution containing 14.5 g of Ni(NO$_3$)$_2$·6H$_2$O and 100 ml of deionized water. After stirring (500 r min^{-1}) for 48 hours at 30°C, the light green products of Ni(OH)$_2$ were separated by filtration, washed with deionized water for 7 times, and dried at 80°C overnight.

Preparation of Ni@Al$_2$O$_3$-IE surrounded catalyst with core-shell structure (by IEIL method)

The Ni@Al$_2$O$_3$-IE surrounded catalysts were prepared by IEIL strategy. Typically, the as-prepared Ni(OH)$_2$ nanosheets (2.0 g) were dispersed in a solution containing aluminum nitrate (11.2 g) and deionized water (60 ml) under stirring at 500 r min^{-1}. Then, the mixture was transferred to a 100-ml Teflon-lined stainless steel autoclave, sealed, and maintained at 120°C for 12 hours. When cooled to room temperature, the resulting precipitate (denoted as NiAl-MMH) was collected by centrifugation, washed with deionized water, and dried at 80°C overnight. After calcination under static air at 400°C for 2 hours, a gray powder (denoted as NiO@Al$_2$O$_3$-IE) was obtained. Last, NiO@Al$_2$O$_3$-IE was reduced in a pure H$_2$ at 500°C for 1 hour with a heating rate of 5°C min^{-1} to yield 16Ni@Al$_2$O$_3$-IE with a nickel loading of 16 wt %. By regulating the Al^{3+}/Ni(OH)$_2$ molar ratio, xNi@Al$_2$O$_3$-IE surrounded catalyst with different nickel loading can be obtained, where x represents the Ni mass percentage determined by inductively coupled plasma atomic emission spectroscopy (ICP-AES).

Preparation of Ni/Al$_2$O$_3$-IE catalyst (by traditional impregnation method)

For comparison, conventional supported Ni-based catalyst with the same loading amount to Ni@Al$_2$O$_3$-IE catalyst, designated as Ni/Al$_2$O$_3$-IM, was prepared by a wet impregnation method. A predetermined amount of Ni(NO$_3$)$_2$·6H$_2$O was dissolved in 30 ml of deionized water, followed by addition of a commercial γ-Al$_2$O$_3$ (surface
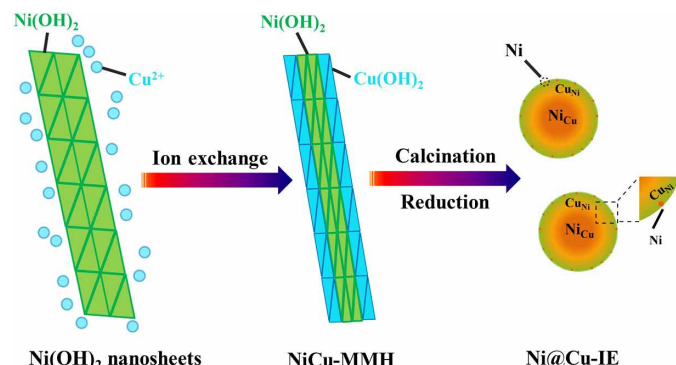

Fig. 6. Schematic diagram toward the synthesis of surrounded Ni@Cu-IE catalyst via the IEIL method.

area of 117 m^2 g^{-1}) and stirred at 30°C for 6 hours, aged for 12 hours, and then dried at 100°C overnight. The calcination and reduction process were consistent with that of Ni@Al$_2$O$_3$-IE.

Note that, in the manuscript, 16Ni@Al$_2$O$_3$-IE and 16Ni/Al$_2$O$_3$-IM samples are chosen to do comparative experiments. For the sake of brevity, in the text, 16Ni@Al$_2$O$_3$-IE and 16Ni/Al$_2$O$_3$-IM are abbreviated as Ni@Al$_2$O$_3$-IE and Ni/Al$_2$O$_3$-IM, respectively.

Preparation of Ni@CeO$_2$-IE surrounded catalysts with inverse structure

The Ni@CeO$_2$-IE catalysts were prepared by IEIL strategy. In a typical procedure for Ni@CeO$_2$-IE (Ce/Ni molar ratio of 0.02), the as-prepared Ni(OH)$_2$ nanosheet (1.8 g) was added into 40 ml of aqueous solution containing 0.17 g of Ce(NO$_3$)$_3$·6H$_2$O under stirring at 500 r min^{-1}. Then, the mixture was transferred to a 50-ml Teflon-lined stainless steel autoclave, sealed, and maintained at 100°C for 4 hours. When cooled to room temperature, the resulting precipitation (denoted as NiCe-MMH) was filtered, washed with deionized water, and dried in an oven at 80°C for overnight followed by calcination and reduction in a 5 volume % H$_2$/N$_2$ stream at 400°C for 2 hours to obtain the Ni@CeO$_2$-IE catalyst with inverse structure. When the initial Ce(NO$_3$)$_3$·6H$_2$O/Ni(OH)$_2$ molar ratio was varied from 0.01 to 0.05, the resulted catalyst was denoted as Ni@0.01CeO$_2$-IE and Ni@0.05CeO$_2$-IE, respectively.

Preparation of Ni/CeO$_2$-IM catalyst

Ni/CeO$_2$-IM catalysts as a reference sample were prepared by wet impregnation of the CeO$_2$ support (2.0 g) (39) with Ni(NO$_3$)$_2$·6H$_2$O solution (10 ml). The slurry was evaporated under stirring at 50°C, dried at 80°C overnight, followed by calcination and reduction under a 5 volume % H$_2$/N$_2$ flow at 400°C for 2 hours to obtain Ni/CeO$_2$-IM catalyst. The Ni loading is 30 wt % to obtain similar Ni particle size as Ni@0.02CeO$_2$-IE.

Note that, in the manuscript, Ni@0.02CeO$_2$-IE and Ni/CeO$_2$-IM samples are chosen to do comparative experiments. For the sake of brevity, Ni@0.02CeO$_2$-IE is abbreviated as Ni@CeO$_2$-IE in the text.

Preparation of Ni@Cu-IE surrounded catalysts with gradient structure

The Ni@Cu-IE catalysts were prepared by IEIL strategy. In a typical procedure, 1.8 g of the as-prepared Ni(OH)$_2$ nanosheet was added into 60 ml of aqueous solution containing 10.8 g of Cu(NO$_3$)$_2$·3H$_2$O under stirring at 500 r min^{-1}. Then, the mixture was transferred to a 100-ml Teflon-lined stainless steel autoclave, sealed, and maintained at 120°C for 4 hours. When cooled to room temperature, the resulting precipitation (NiCu-MMH) was filtered, washed with deionized water, dried in an oven at 80°C for overnight, and followed by calcination and reduction in a 5 volume % H$_2$/N$_2$ stream at a different temperature for 2 hours to obtain the Ni@Cu-IE-r (r = 350, 400, 450, and 500) catalysts with gradient structure. For the sake of brevity, Ni@Cu-IE-500 is abbreviated as Ni@Cu-IE in the text.

Characterizations

The chemical composition of the solids was determined ICP-AES (Optima 5300DV). XRD patterns were recorded on a Philips X′Pert XRD with Co Kα radiation (35 kV, 40 mA, λ = 1.7902 Å).

The morphology of products was characterized by scanning electron microscopy (Hitachi S-4800). The TEM images were obtained using a JEOL JEM-1010 electron microscope operated at 100 kV.

High-angle annular dark-field scanning TEM was performed in the JEOL ARM 200F equipped with double aberration correctors and cold field emission gun operated at 200 kV.

XPS analysis was undertaken on a PHI 5000 VersaProbe system using a monochromatic Al Kα x-ray source. All binding energies were referenced to the C 1s line at 284.6 eV.

H$_2$-TPR, NH$_3$-TPD, CO-TPD, H$_2$ pulse chemisorption, and CO pulse chemisorption were carried out on a FINESORB-3010 instrument equipped with a thermal conductivity detector (TCD). Typically, before the TPR measurements, the sample (50 mg in all runs) was pretreated at 300°C for 30 min under Ar flow to remove any absorbed gases. Then, the sample was cooled to room temperature, followed by heating to 900°C at a rate of 10°C min^{-1} in a 5% H$_2$/Ar gas flow (20 ml min^{-1}). For NH$_3$-TPD and CO-TPD, 0.1 g of samples was prereduced in situ by 5%H$_2$/Ar flow and saturated with NH$_3$ or CO for 1 hour at 100°C and room temperature, respectively. After the physically adsorbed NH$_3$ or CO was removed by flushing with He for 1 hour, the sample was heated to 600° and 900°C in He flow, respectively. Before H$_2$ or CO pulse chemisorption, 150 mg of sample was first prereduced by 5% H$_2$/Ar flow at 500° or 400°C for 2 hour, followed by flushing with pure Ar or He for 1 hour, and then the temperature was decreased to 30°C. Subsequently, successive H$_2$ or CO pulses were introduced until a stable TCD single was obtained.

TG analysis was carried out on a NETZSCH STA 449 C instrument. The patterns were registered from room temperature to 900°C with a heating rate of 10°C min^{-1} in air.

Activity evaluation of the catalysts on CO methanation

Catalytic performances for CO methanation were investigated in a stainless-steel tubular microreactor with an inner diameter of 10 mm. About 0.2 g of catalyst was used for each test. The catalysts were reduced at 500°C for 1 hour in 20 ml min^{-1} H$_2$. After reduction, the feed gas was introduced to the reactor with a $V(H_2)/V(CO)$ ratio of 3:1. The reaction was performed at 1.0 MPa and a WHSV of 25,000 ml g^{-1} $hour^{-1}$ in the temperature region of 200° to 500°C; in addition, the long-term tests were set at 500°C with a WHSV of 100,000 ml g^{-1} $hour^{-1}$ to distinguish the difference of the catalysts. For the calculation of TOF, a WHSV of 100,000 ml g^{-1} $hour^{-1}$ is used to keep the total CO conversion below 10%. The products were separated and analyzed on line by GC (GC900D).

Activity evaluation of the catalysts on transfer hydrogenation of nitrobenzene

The transfer hydrogenation of nitrobenzene was carried out in a 25-ml Teflon-lined stainless steel autoclave with magnetic stirring. In a typical reaction, catalyst (C_{Ni} of 30 mM^{-1}), nitrobenzene (0.5 mmol), solvent (8 ml; V_{EtOH}/V_{H2O} = 3:1), and 20 μl of anisole as a standard were added into the reactor. Then, hydrazine hydrate and the catalysts were introduced and filled with argon. The mixture was vigorously stirred (~1000 rpm) at 60°C for 1 hour. After the reaction, the samples were rapidly separated by a magnet, and the products were analyzed by GC (GC-9860) with a capillary column and a flame ionization detector (FID).

Activity evaluation of the catalysts on semihydrogenation of phenylacetylene

The semihydrogenation of phenylacetylene was carried out in a 25-ml Teflon-lined stainless steel autoclave with magnetic stirring. In a typical reaction, the catalysts (30 mg), phenylacetylene (1.0 mmol), ethanol (8 ml), and 20 μl of decane as a standard were added into the reactor. The autoclave was purged three times with H$_2$ and then pressurized to 1.0 MPa. The mixture was vigorously stirred

(~1000 rpm) at 70°C for 2 hours. After the reaction, the samples were rapidly separated by a magnet, and the products were analyzed by GC (GC-9860) with a capillary column and an FID.

SUPPLEMENTARY MATERIALS

Supplementary material for this article is available at http://advances.sciencemag.org/cgi/content/full/6/20/eaay7031/DC1

REFERENCES AND NOTES

1. N. Mizuno, M. Misono, Heterogeneous catalysis. *Chem. Rev.* **98**, 199–218 (1998).
2. A. D. O. Cinneide, J. K. A. Clarke, Catalysis on supported metals. *Catal. Rev.* **7**, 213–232 (1972).
3. Q. Fu, F. Yang, X. Bao, Interface-confined oxide nanostructures for catalytic oxidation reactions. *Acc. Chem. Res.* **46**, 1692–1701 (2013).
4. S. J. Tauster, S. C. Fung, R. L. Garten, Strong metal-support interactions. Group 8 noble metals supported on titanium dioxide. *J. Am. Chem. Soc.* **100**, 170–175 (1978).
5. M. Cargnello, V. V. T. Doan-Nguyen, T. R. Gordon, R. E. Diaz, E. A. Stach, R. J. Gorte, P. Fornasiero, C. B. Murray, Control of metal nanocrystal size reveals metal-support interface role for ceria catalysts. *Science* **341**, 771–773 (2013).
6. S. Kattel, P. J. Ramírez, J. G. Chen, J. A. Rodriguez, P. Liu, Active sites for CO₂ hydrogenation to methanol on Cu/ZnO catalysts. *Science* **355**, 1296–1299 (2017).
7. M. McEntee, W. Tang, M. Neurock, J. T. Yates Jr., Selective catalytic oxidative-dehydrogenation of carboxylic acids-acrylate and crotonate formation at the Au/TiO₂ interface. *J. Am. Chem. Soc.* **136**, 5116–5120 (2014).
8. G. Kennedy, G. Melaet, H.-L. Han, W. T. Ralston, G. A. Somorjai, In situ spectroscopic investigation into the active sites for crotonaldehyde hydrogenation at the Pt nanoparticle-Co₃O₄ interface. *ACS Catal.* **6**, 7140–7147 (2016).
9. N. M. Briggs, L. Barrett, E. C. Wegener, L. V. Herrera, L. A. Gomez, J. T. Miller, S. P. Crossley, Identification of active sites on supported metal catalysts with carbon nanotube hydrogen highways. *Nat. Commun.* **9**, 3827–3834 (2018).
10. T. Whittaker, K. B. S. Kumar, C. Peterson, M. N. Pollock, L. C. Grabow, B. D. Chandler, H₂ oxidation over supported Au nanoparticle catalysts: Evidence for heterolytic H₂ activation at the metal-support interface. *J. Am. Chem. Soc.* **140**, 16469–16487 (2018).
11. Q. Fu, W. Li, Y. Yao, H. Liu, H. Y. Su, D. Ma, X. K. Gu, L. Chen, Z. Wang, H. Zhang, B. Wang, X. Bao, Interface-confined ferrous centers for catalytic oxidation. *Science* **328**, 1141–1144 (2010).
12. J. Lu, B. Fu, M. C. Kung, G. Xiao, J. W. Elam, H. H. Kung, P. C. Stair, Coking-and sintering-resistant palladium catalysts achieved through atomic layer deposition. *Science* **335**, 1205–1208 (2012).
13. K. Cheng, W. Zhou, J. Kang, S. He, S. Shi, Q. Zhang, Y. Pan, W. Wen, Y. Wang, Bifunctional catalysts for one-step conversion of syngas into aromatics with excellent selectivity and stability. *Chem* **3**, 334–347 (2017).
14. I. Ro, J. Resasco, P. Christopher, Approaches for understanding and controlling interfacial effects in oxide-supported metal catalysts. *ACS Catal.* **8**, 7368–7387 (2018).
15. J.-W. Yang, W.-T. Zheng, Z. Hu, M. Zhang, B.-Q. Xu, Do Olefin hydrogenation reactions remain structure insensitive over Pt in nanostructured Pt-on-Au catalyst? *ACS Catal.* **8**, 10254–10260 (2018).
16. L. B. Vilhelmsen, B. Hammer, Identification of the catalytic site at the interface perimeter of Au clusters on rutile TiO₂(110). *ACS Catal.* **4**, 1626–1631 (2014).
17. T. P. Senftle, A. C. T. van Duin, M. J. Janik, Methane activation at the Pd/CeO₂ interface. *ACS Catal.* **7**, 327–332 (2017).
18. M. Xu, S. Yao, D. Rao, Y. Niu, N. Liu, M. Peng, P. Zhai, Y. Man, L. Zheng, B. Wang, B. Zhang, D. Ma, M. Wei, Insights into interfacial synergistic catalysis over Ni@TiO₂₋ₓ catalyst toward water-gas shift reaction. *J. Am. Chem. Soc.* **140**, 11241–11251 (2018).
19. A. Chen, X. Yu, Y. Zhou, S. Miao, Y. Li, S. Kuld, J. Sehested, J. Liu, T. Aoki, S. Hong, M. F. Camellone, S. Fabris, J. Ning, C. Jin, C. Yang, A. Nefedov, C. Wöll, Y. Wang, W. Shen, Structure of the catalytically active copper-ceria interfacial perimeter. *Nat. Catal.* **2**, 334–341 (2019).
20. G. Chen, Y. Zhao, G. Fu, P. N. Duchesne, L. Gu, Y. Zheng, X. Weng, M. Chen, P. Zhang, C. W. Pao, J. F. Lee, N. Zheng, Interfacial effects in iron-nickel hydroxide-platinum nanoparticles enhance catalytic oxidation. *Science* **344**, 495–499 (2014).
21. X. P. Fu, L. W. Guo, W. W. Wang, C. Ma, C. J. Jia, K. Wu, R. Si, L. D. Sun, C. H. Yan, Direct identification of active surface species for the water-gas shift reaction on a gold-ceria catalyst. *J. Am. Chem. Soc.* **141**, 4613–4623 (2019).
22. C. Xu, G. Chen, Y. Zhao, P. Liu, X. Duan, L. Gu, G. Fu, Y. Yuan, N. Zheng, Interfacing with silica boosts the catalysis of copper. *Nat. Commun.* **9**, 3367–3377 (2018).
23. N. Liu, M. Xu, Y. Yang, S. Zhang, J. Zhang, W. Wang, L. Zheng, S. Hong, M. Wei, Au^δ⁻-Oᵥ-Ti³⁺ interfacial site: Catalytic active center toward low-temperature water gas shift reaction. *ACS Catal.* **9**, 2707–2717 (2019).
24. Y. Dai, B. Lim, Y. Yang, C. M. Cobley, W. Li, E. C. Cho, B. Grayson, P. T. Fanson, C. T. Campbell, Y. Sun, Y. Xia, A sinter-resistant catalytic system based on platinum nanoparticles supported on TiO₂ nanofibers and covered by porous silica. *Angew. Chem. Int. Ed. Engl.* **49**, 8165–8168 (2010).
25. L. Cao, W. Liu, Q. Luo, R. Yin, B. Wang, J. Weissenrieder, M. Soldemo, H. Yan, Y. Lin, Z. Sun, C. Ma, W. Zhang, S. Chen, H. Wang, Q. Guan, T. Yao, S. Wei, J. Yang, J. Lu, Atomically dispersed iron hydroxide anchored on Pt for preferential oxidation of CO in H₂. *Nature* **565**, 631–635 (2019).
26. P. Munnik, P. E. de Jongh, K. P. de Jong, Recent developments in the synthesis of supported catalysts. *Chem. Rev.* **115**, 6687–6718 (2015).
27. E. C. Kruissink, L. L. van Reijen, J. R. H. Ross, Coprecipitated nickel-alumina catalysts for methanation at high temperature. Part 1.—Chemical composition and structure of the precipitates. *J. Chem. Soc. Faraday Trans.* **77**, 649–663 (1981).
28. C. Mirodatos, H. Praliaud, M. Primet, Deactivation of nickel-based catalysts during CO methanation and disproportionation. *J. Catal.* **107**, 275–287 (1987).
29. Q. Liu, Z. Zhong, F. Gu, X. Wang, X. Lu, H. Li, G. Xu, F. Su, CO methanation on ordered mesoporous Ni-Cr-Al catalysts: Effects of the catalyst structure and Cr promoter on the catalytic properties. *J. Catal.* **337**, 221–232 (2016).
30. Y. Zhang, X. Weng, H. Li, H. Li, M. Wei, J. Xiao, Z. Liu, M. Chen, Q. Fu, X. Bao, Hexagonal boron nitride cover on Pt(111): A new route to tune molecule–Metal interaction and metal-catalyzed reactions. *Nano Lett.* **15**, 3616–3623 (2015).
31. L. Gao, Q. Fu, M. Wei, Y. Zhu, Q. Liu, E. Crumlin, Z. Liu, X. Bao, Enhanced nickel-catalyzed methanation confined under hexagonal boron nitride shells. *ACS Catal.* **6**, 6814–6822 (2016).
32. C. Jia, J. Gao, J. Li, F. Gu, G. Xu, Z. Zhong, F. Su, Nickel catalysts supported on calcium titanate for enhanced CO methanation. *Cat. Sci. Technol.* **3**, 490–499 (2013).
33. P. Munnik, M. E. Z. Velthoen, P. E. de Jongh, K. P. de Jong, C. J. Gommes, Nanoparticle growth in supported nickel catalysts during methanation reaction—Larger is better. *Angew. Chem. Int. Ed.* **53**, 9493–9497 (2014).
34. M. N. Pahalagedara, L. R. Pahalagedara, J. He, R. Miao, B. Gottlieb, D. Rathnayake, S. L. Suib, Room temperature selective reduction of nitrobenzene to azoxybenzene over magnetically separable urchin-like Ni/Graphene nanocomposites. *J. Catal.* **336**, 41–48 (2016).
35. L. Wang, E. Guan, J. Zhang, J. Yang, Y. Zhu, Y. Han, M. Yang, C. Cen, G. Fu, B. C. Gates, F. S. Xiao, Single-site catalyst promoters accelerate metal-catalyzed nitroarene hydrogenation. *Nat. Commun.* **9**, 1362 (2018).
36. S. Zhang, C. R. Chang, Z. Q. Huang, J. Li, Z. Wu, Y. Ma, Z. Zhang, Y. Wang, Y. Qu, High catalytic activity and chemoselectivity of sub-nanometric Pd clusters on porous nanorods of CeO₂ for hydrogenation of nitroarenes. *J. Am. Chem. Soc.* **138**, 2629–2637 (2016).
37. J. Hu, Z. Zhou, R. Zhang, L. Li, Z. Cheng, Selective hydrogenation of phenylacetylene over a nano-Pd/α-Al₂O₃ catalyst. *J. Mol. Catal. A-Chem.* **381**, 61–69 (2014).
38. M. Xie, S. Duan, Y. Shen, K. Fang, Y. Wang, M. Lin, X. Guo, In-situ-grown Mg(OH)₂-derived hybrid α-Ni(OH)₂ for highly stable supercapacitor. *ACS Energy Lett.* **1**, 814–819 (2016).
39. T. Hou, Y. Wang, J. Zhang, M. Li, J. Lu, M. Heggen, C. Sievers, F. Wang, Peculiar hydrogenation reactivity of Ni-Ni^δ⁺ clusters stabilized by ceria in reducing nitrobenzene to azoxybenzene. *J. Catal.* **353**, 107–115 (2017).
40. P. L. Benito, A. G. Gayubo, A. T. Aguayo, M. Olazar, J. Bilbao, Deposition and characteristics of coke over a H-ZSM5 Zeolite-based catalyst in the MTG process. *Ind. Eng. Chem. Res.* **35**, 3991–3998 (1996).
41. I. Czekaj, F. Loviat, F. Raimondi, J. Wambach, S. Biollaz, A. Wokaun, Characterization of surface processes at the Ni-based catalyst during the methanation of biomass-derived synthesis gas: X-ray photoelectron spectroscopy (XPS). *Appl. Catal. Gen.* **329**, 68–78 (2007).
42. C. H. Bartholomew, Mechanisms of catalyst deactivation. *Appl. Catal. Gen.* **212**, 17–60 (2001).
43. Z. Li, L. Mo, Y. Kathiraser, S. Kawi, Yolk–Satellite–Shell structured Ni–Yolk@Ni@SiO₂ nanocomposite: Superb catalyst toward Methane CO₂ reforming reaction. *ACS Catal.* **4**, 1526–1536 (2014).
44. A. Kumar, S. Babu, A. S. Karakoti, A. Schulte, S. Seal, Luminescence properties of europium-doped cerium oxide nanoparticles: Role of vacancy and oxidation states. *Langmuir* **25**, 10998–11007 (2009).
45. M. L. Ang, U. Oemar, E. T. Saw, L. Mo, Y. Kathiraser, B. H. Chia, S. Kawi, Highly active Ni/xNa/CeO₂ catalyst for the water–Gas shift reaction: Effect of sodium on methane suppression. *ACS Catal.* **4**, 3237–3248 (2014).

Citation: P. Hao, M. Xie, S. Chen, M. Li, F. Bi, Y. Zhang, M. Lin, X. Guo, W. Ding, X. Guo, Surrounded catalysts prepared by ion-exchange inverse loading. *Sci. Adv.* **6**, eaay7031 (2020).